PHYSICAL REVIEW A **83**, 062702 (2011)

# Double ionization of helium by bare ions: Theoretical study of the fully differential cross sections

S. D. López,[1,*] C. R. Garibotti,[1] and S. Otranto[2]
[1]*Consejo Nacional de Investigaciones Cientificas y Tecnicas and Centro Atómico Bariloche, Avenida Bustillo 9400, 8400 San Carlos de Bariloche, Argentina*
[2]*Instituto de Física del Sur and Departamento de Física, Universidad Nacional del Sur, 8000 Bahía Blanca, Argentina*

(Received 28 March 2011; published 13 June 2011)

This work presents a theoretical study of fully differential cross sections (FDCSs) for the double ionization of an He target by ion impact within a distorted wave model. The initial atomic system is described by two approximated wave functions of different accuracy proposed by Bonham and Kohl. For the final channel several models are considered based upon improvements and simplifications of the well-known three-body Coulomb (3C) model. The influence of the receding projectile on the resulting fragments is also studied by implementing a model with effective charges that depend on the momenta of the four particles. The FDCSs resulting for different electron energy sharing are discussed. The sensitivity of the FDCSs to the projectile charge sign and magnitude is explored over the energy range 700 keV/amu through 6 MeV/amu.

DOI: 10.1103/PhysRevA.83.062702 PACS number(s): 34.50.Fa, 34.10.+x

## I. INTRODUCTION

Atomic collision processes involving two or more electrons have shown to be relevant not only to the atomic physics community but also to other fields such as astrophysics and radiotherapy. In the astrophysics context we can cite the important contribution to the x-ray spectra emission of double capture processes to highly excited states followed by autoionization or double radiative decay. These processes take place in collisions involving low-energy solar wind ions as they transit planetary atmospheres or cometary comas [1,2]. Concerning radiotherapy applications, we emphasize how important it is to describe multiple ionization as well as transfer ionization processes accurately in order to provide confident data to the Monte Carlo codes used to describe the dose distribution [3].

In particular, experimental studies of the double ionization (DI) of He by proton impact were performed in the early 1980s [4,5] and mainly concentrated in total cross sections $\sigma^{2+}$ and the experimental determination of the ratio $R = \sigma^{2+}/\sigma^{+}$. The $R$ values obtained for He targets by proton and antiproton impact showed clear differences even at large impact energies where first Born-type approximations were already reliable for $\sigma^{+}$. In those days, two theoretical models successfully reproduced the proton-antiproton magnitude difference for $R$: the forced impulse method [6] and the $n$ body classical trajectory Monte Carlo ($n$CTMC) model [7]. Most of the quantum mechanical calculations of $\sigma^{2+}$ for light targets such as He and Li were performed within the independent electron (IEL) model [8,9] or the independent event (IEV) model [9,10]. None of these models provided an ultimate description of $\sigma^{2+}$ at the whole range of collision energies experimentally explored [10–14].

A great experimental advance in the process took place with the introduction of the cold target recoil ion momentum spectroscopy (COLTRIMS) technique by the mid 1990s [15]. As a result, and following by a couple of years the measurement of similar ($e$,3$e$) data by the same group [16], in 2003 the first fully differential cross sections (FDCSs) of the He collisional breakup process by 6-MeV protons were presented and compared to their electron-impact counterparts [17]. From those studies the authors concluded that even for double ionizing collisions involving intermediate- to low-momentum transfers, the projectile charge sign played a major role at the large impact velocity explored of 15.5 a.u.

These experimental results were later integrated and presented in terms of doubly differential cross sections (DDCSs) [18]. Nonperturbative close-coupling time-dependent methods recently succeeded to accurately reproduce these angular DDCSs [19,20].

Let's now briefly describe the distorted wave models employed so far to calculate the double ionization FDCSs and DDCSs. These models have been built upon initial-state wave functions, which only consider radial correlation, and final-state wave functions based on the independent particle 2C model. The interaction between the emitted electrons is introduced in those works by means of correlation factors (Ward-Macek type [21] and Gamow, respectively) that are $r_{12}$ independent or consider $r_{12}$ as a momentum-dependent fixed parameter. Lobanova *et al.* have only retained the first-order amplitude [22], while Ciappina *et al.* have added an approximate second-order mechanism (noncoherently) at the squared amplitude level [23,24]. The approximations inherent to these methods drastically decrease the numerical cost involved. As a result, a large set of FDCSs can be computed, allowing for an appropriate convolution over the reported uncertainties. In contrast, none of these models can provide information on the possible differences arising in collisions involving positively and negatively charged projectiles, since they include at most terms proportional to $Z_P^2$ and $Z_P^4$.

In this paper, we explore the theoretical description of FDCSs for the double ionization of He by positive bare ions with charges $Z = 1+$ to $6+$ as well as by antiprotons in the energy range 700 keV/amu through 6 MeV/amu ($V \approx 5.29 - 15.5$ a.u.). The goal of this work is twofold. First, we consider the projectile as a plane wave in both initial and final channels and compare the FDCSs obtained by using two variational initial wave functions of different accuracy together with analytical wave functions proposed for

---

[*] sebastian.lopez@cab.cnea.gov.ar

the three-body continuum. Second, we explore the projectile charge sign and magnitude dependence at the fully differential level by introducing a model based on effective charges similar to that introduced by Jetzke and Faisal in their electron and positron atom studies [25]. The usual contour plots that have become familiar in these sorts of studies are presented together with selected cuts in order to help visualize the main physical trends. Finally, conclusions are drawn and future work lines mentioned. Atomic units are used throughout this work unless explicitly stated.

## II. THEORY

We consider the double ionization of a He atom by an ion with initial (final) momentum $\mathbf{K}_i$ ($\mathbf{K}_f$) and we denote $\mathbf{k}_1$ and $\mathbf{k}_2$ the momenta of the emitted electrons relative to the target. Our study will be restricted to fast ions that during the collision process transfer an intermediate to low amount of momentum. In this context, we initially represent the projectile in the initial and final states by plane waves. The FDCS for the double ionization process is defined as

$$\frac{d\sigma}{d\mathbf{k}_1 d\mathbf{k}_2 d\mathbf{Q}_\perp} = \frac{(2\pi)^4}{V^2}|T_{fi}|^2. \tag{1}$$

Here, $\mathbf{Q}_\perp$ is the perpendicular component of the momentum transferred by the projectile defined by $\mathbf{Q} = \mathbf{K}_i - \mathbf{K}_f$. The transition amplitude in the distorted wave formalism at first order $T_{fi}$ is given by

$$T_{fi} = \langle \chi_f^- | W_i | \chi_i^+ \rangle. \tag{2}$$

We now describe the wave functions and operators used throughout this work. The initial state $\chi_i^+$ is given by,

$$\chi_i^+ = \frac{1}{(2\pi)^{3/2}} e^{i\mathbf{K}_i\cdot\mathbf{R}} \Psi_i^+(\mathbf{r}_1,\mathbf{r}_2). \tag{3}$$

Here, $\mathbf{r}_1$ and $\mathbf{r}_2$ are the positions of the electrons relative to the target, $\mathbf{r}_{12} = \mathbf{r}_1 - \mathbf{r}_2$ and $\mathbf{R}$ is the distance between the ions. For the He($1s^2$) ground-state wave function ($\Psi_i^+$), we consider two wave functions:

(i) The Bonham and Kohl wave function 7 [hereafter termed ground state 1 (GS1)], (see Table I in Ref. [26]), which only includes radial correlation among the bound electrons,

$$\Psi_i^+(\mathbf{r}_1,\mathbf{r}_2) = N_i(e^{-\alpha r_1 - \beta r_2} + e^{-\beta r_1 - \alpha r_2}). \tag{4}$$

The normalization constant and the variational parameters are $N_i = 0.708\,92$, $\alpha = 2.1832$, and $\beta = 1.1885$ . This wave function leads to an energy $< E >= -2.8756$ a.u., close to the denominated radial limit of $-2.879$ a.u., which is the energy limit that can be reached by only including radial correlation in the wave function.

(ii) The Bonham and Kohl wave function 9 (GS2) as adapted by Otranto *et al.* [27]

$$\Psi_i^+(\mathbf{r}_1,\mathbf{r}_2) = N_i(e^{-ar_1 - br_2} + e^{-br_1 - ar_2})(e^{-z_c r_{12}} + C_0 e^{-\lambda r_{12}}), \tag{5}$$

where $N_i = 1.9358$, $a = 1.4126$, $b = 2.2068$, $\lambda = 0.199$, $C_0 = -0.6649$, and $z_c = 0.01$. This wave function includes angular correlation (through the explicit $r_{12}$ dependence) and leads to an energy $< E >= -2.9019$ a.u, only 0.0489 eV apart from the exact energy $-2.9037$ a.u. [27]. This wave function differs from the original Bonham and Kohl wave function in the $e^{-z_c r_{12}}$ factor which replaces 1 in the original function. This value was introduced to avoid spurious convergence factors usually introduced to compute cross sections. In that work, all the variational parameters were recalculated for the He isoelectronic sequence up to $Z_T = 10$.

The operator $W_i$ represents the unsolved part of the initial Hamiltonian and reads

$$W_i = \frac{Z_P Z_T}{R} - \frac{Z_P}{|\mathbf{R} - \mathbf{r}_1|} - \frac{Z_P}{|\mathbf{R} - \mathbf{r}_2|}. \tag{6}$$

For the final continuum state, after the two electrons have been emitted from the target, we will use the following models:

(i) The 2C-$C(\mathbf{k}_{12})$ model [11,12,22,23]:

$$\chi_f^- = \frac{1}{(2\pi)^{3/2}} e^{i\mathbf{K}_f\cdot\mathbf{R}} \Psi_f^-, \tag{7}$$

$$\begin{aligned}\Psi_f^- = \frac{1}{(2\pi)^3}\frac{(1+P_{12})}{\sqrt{2}}&[e^{i(\mathbf{k}_1\cdot\mathbf{r}_1 + \mathbf{k}_2\cdot\mathbf{r}_2)} D_{\mathbf{k}_1}(\eta_1,\mathbf{r}_1)\\ &\times D_{\mathbf{k}_2}(\eta_2,\mathbf{r}_2)]C(\mathbf{k}_{12}),\end{aligned} \tag{8}$$

where $P_{12}$ is the permutation operator and $C(\mathbf{k}_{12})$ is a correlation factor which depends on the interelectronic momentum $\mathbf{k}_{12}$. Here, $\eta_1 = -Z_T/k_1$ and $\eta_2 = -Z_T/k_2$are the corresponding Sommerfeld parameters.

(ii) The three-body Coulomb (3C) model [28,29]:

$$\chi_f^- = \frac{1}{(2\pi)^{3/2}} e^{i\mathbf{K}_f\cdot\mathbf{R}} \Psi_f^-, \tag{9}$$

$$\begin{aligned}\Psi_f^- = \frac{1}{(2\pi)^3}\frac{(1+P_{12})}{\sqrt{2}}&[e^{i(\mathbf{k}_1\cdot\mathbf{r}_1 + \mathbf{k}_2\cdot\mathbf{r}_2)} D_{\mathbf{k}_1}(\eta_1,\mathbf{r}_1)\\ &\times D_{\mathbf{k}_2}(\eta_2,\mathbf{r}_2) D_{\mathbf{k}_{12}}(\eta_{12},\mathbf{r}_{12})],\end{aligned} \tag{10}$$

where $D_{\mathbf{k}}(\eta,\mathbf{r})$ is the Coulomb distortion factor

$$D_{\mathbf{k}}(\mathbf{r}) = \Gamma(1 - i\eta)e^{-\frac{\pi\eta}{2}}\,{}_1F_1\,[i\eta, 1, -i(kr + \mathbf{k}\cdot\mathbf{r})], \tag{11}$$

and the interelectronic Sommerfeld parameter is given by $\eta_{12} = 1/(2k_{12})$ with $\mathbf{k}_{12} = (\mathbf{k}_1 - \mathbf{k}_2)/2$ . This model explicitly considers the interactions among the three particles but neglects the nonorthogonal kinetic energy given by the nondiagonal elements of the metric tensor. The 3C wave function leads to a description of the three-body continuum in which the different pairs of particles act unaware of the third particle under consideration. The lack of nonorthogonal kinetic energy becomes clearly evident in the usually denominated Wannier limit, in which the electrons are emitted almost collinear and with very low energy. The 3C model leads to an exponential underestimation of the cross sections as the electrons' emission energy decreases in contrast to the expected power-law dependence predicted by Wannier theories [30].

(iii) The dynamical screening (DS) models: Many studies were performed during the 1990s with the aim of improving the 3C model [31–35]. All these studies had the common purpose of obtaining a more accurate analytical wave function for the three-body Coulomb problem. Although these models have shown partial success in different contexts (electron impact studies, ion-impact studies, photo-double ionization) and for different energy ranges, none of them has arisen in subsequent studies as the ultimate analytical wave function. For two low-energy electrons in the continuum, the effective charges model of Berakdar and Briggs has shown some success in $(e,2e)$ and $(e,3e)$ studies [32,33,36]. For each pair of particles these effective charges are

$$\begin{aligned} Z^{\mathrm{DS}}_{e_1-He^+} &= -Z_T + Z_{\mathrm{eff}_1}(k_1,k_2,k_{12}) \\ Z^{\mathrm{DS}}_{e_2-He^+} &= -Z_T + Z_{\mathrm{eff}_2}(k_1,k_2,k_{12}) \\ Z^{\mathrm{DS}}_{e_1-e_2} &= 1 - Z_{\mathrm{eff}_{12}}(k_1,k_2,k_{12}) \end{aligned} \tag{12}$$

with

$$\begin{aligned} Z_{\mathrm{eff}_1}(k_1,k_2,k_{12}) &= \left(\frac{3+\cos^2 4\alpha_1}{4}\frac{k_1}{k_1+k_2}\right)^2 \frac{k_{12}}{k_1+k_2} \\ Z_{\mathrm{eff}_2}(k_1,k_2,k_{12}) &= \left(\frac{3+\cos^2 4\alpha_2}{4}\frac{k_2}{k_1+k_2}\right)^2 \frac{k_{12}}{k_1+k_2} \\ Z_{\mathrm{eff}_{12}}(k_1,k_2,k_{12}) &= \left(\frac{3+\cos^2 4\alpha_1}{4}\frac{k_{12}}{k_1+k_2}\right)^2 \frac{k_1}{k_1+k_2} \\ &\quad + \left(\frac{3+\cos^2 4\alpha_2}{4}\frac{k_{12}}{k_1+k_2}\right)^2 \frac{k_2}{k_1+k_2} \end{aligned} \tag{13}$$

and the coefficients $\alpha_1$ and $\alpha_2$ being given by

$$\alpha_1 = \arccos\frac{k_2}{\sqrt{k_1^2+k_2^2}} \qquad \alpha_2 = \arccos\frac{k_1}{\sqrt{k_1^2+k_2^2}}. \tag{14}$$

These charges were initially derived as coordinate dependent and they satisfy a certain number of desired asymptotic limits. The above shown momentum-dependent charges are obtained when the ansatz $r_i \to k_i t$ is assumed [33]. These charges are much easier to implement from the computational view compared to the coordinate-dependent charges since they allow the partial use of Nordsieck-type integrals that clearly alleviate the numerical work to be performed.

(iv) The DS3C-GO model: The previous models for the final state only focused on the two-electron continuum of the atomic system. The possible influence of the receding projectile on this subsystem has been neglected so far. A simple extension, from the analytical point of view, would be to increase the number of Coulomb waves and distortion factors in order to deal with a 6C model. This model has been used in the $(e,3e)$ context by Götz and Briggs [36] and considers all the two-body interactions between the particles in the final channel and hence goes beyond a second Born series. However, the amount of calculation needed (9-$D$ integrals) only allowed the calculation of a few FDCSs as stated by the authors and their conclusions are still the focus of debate [37].

A simpler alternative that we explore in this work, still preserving the Götz and Briggs strategy, is the introduction of the Jetzke-Faisal first-order multiple scattering model [25]. In the ion-atom context its implementation results in the nuclear-nuclear interaction being explicitly included in the final state through a Coulomb wave function:

$$\chi_f^- = \frac{1}{(2\pi)^{3/2}} e^{i\mathbf{K}_f\cdot\mathbf{R}} D_{\mathbf{K}_f}(\eta_{\mathrm{NN}},\mathbf{R})\Psi_f^{\,-}. \tag{15}$$

Furthermore, effective charges are introduced following Jetzke and Faisal, in order to include the projectile charge effects on the electrons' dynamics. Such a strategy was previously considered by Gasaneo *et al.* for $(e,3e)$ processes [38] and was used on a He target at intermediate- to high-impact energies. The effective charges that are used in this work are then given by

$$\begin{aligned} Z^{\mathrm{GO}}_{e_{1-He}} &= Z^{\mathrm{DS}}_{e_1-He^+} + Z_P\frac{\mathbf{k}_{1P}.\mathbf{k}_1}{k_{1P}^3}k_1 \\ Z^{\mathrm{GO}}_{e_{2-He}} &= Z^{\mathrm{DS}}_{e_2-He^+} + Z_P\frac{\mathbf{k}_{2P}.\mathbf{k}_2}{k_{2P}^3}k_2 \\ Z^{\mathrm{GO}}_{e_1-e_2} &= Z^{\mathrm{DS}}_{e_1-e_2} \\ Z_{\mathrm{PT}} &= Z_P\left(Z_T + \frac{\mathbf{k}_{1P}.\mathbf{V}}{k_{1P}^3}V + \frac{\mathbf{k}_{2P}.\mathbf{V}}{k_{2P}^3}V\right). \end{aligned} \tag{16}$$

As a result, the charges seen by the electrons in the DSC model of Berakdar and Briggs are corrected with terms that explicitly consider the projectile charge as well as the relative velocities of the emitted electrons with respect to the projectile [38]. Here, $\mathbf{k}_{1P}$ and $\mathbf{k}_{2P}$ are the electrons' momenta relative to the projectile and $\mathbf{V}$ is the velocity of the projectile.

For $Z_P > 0$ and $v_P > k_1, \sim k_2$ the target core charge seen by each of the electrons is lowered, depending on how fast and in which direction each electron is emitted. For $Z_P < 0$ and $v_P > k_1, \sim k_2$ opposite conclusions apply: The target core charge seen by the electrons increases depending on each relative velocity with respect to the projectile. As we can see, for large impact energies and low electron emission energies these charges tend to $Z_T$ as $1/k_{1P}^2$ irrespective of the charge sign or magnitude of $Z_P$. As the impact energy is lowered, the sign and magnitude of $Z_P$ plays a role affecting the core charge seen by the ejected electrons as well as the internuclear charge.

The fact that these charges are momentum dependent allows, within the present calculation scheme, the computation of a wide set of FDCSs and provides, in this sense, a larger bench test for the model. The introduction of these effective charges provides some information on the possible differences arising in collisions involving positively and negatively charged projectiles. In this sense, the present model allows the exploration of the projectile charge sign dependence predicted by Fischer *et al.* [17] at the fully differential level. However, the convolution over the reported experimental uncertainties turns prohibitive within the DS3C-GO model due to the numerical cost involved. Thus, representative punctual emission energies and momentum transfers are considered and discussed in the next section.

## III. RESULTS

First, we will model the impinging projectile in terms of plane waves and we concentrate on the description of the He subsystem provided by the different models. We describe the calculated FDCSs for double ionization of He by proton impact in the coplanar emission geometry ($\mathbf{Q}$,$\mathbf{k}_1$ and $\mathbf{k}_2$ all laying in the scattering plane). The FDCS will be represented in terms of contour plots as a function of the electron emission angles $\theta_1$ and $\theta_2$ with respect to the forward beam direction. In the following, we denote the different combinations of initial and final wave functions under study by means of their respective acronyms introduced above. In Figs. 1(a)–1(d) we show

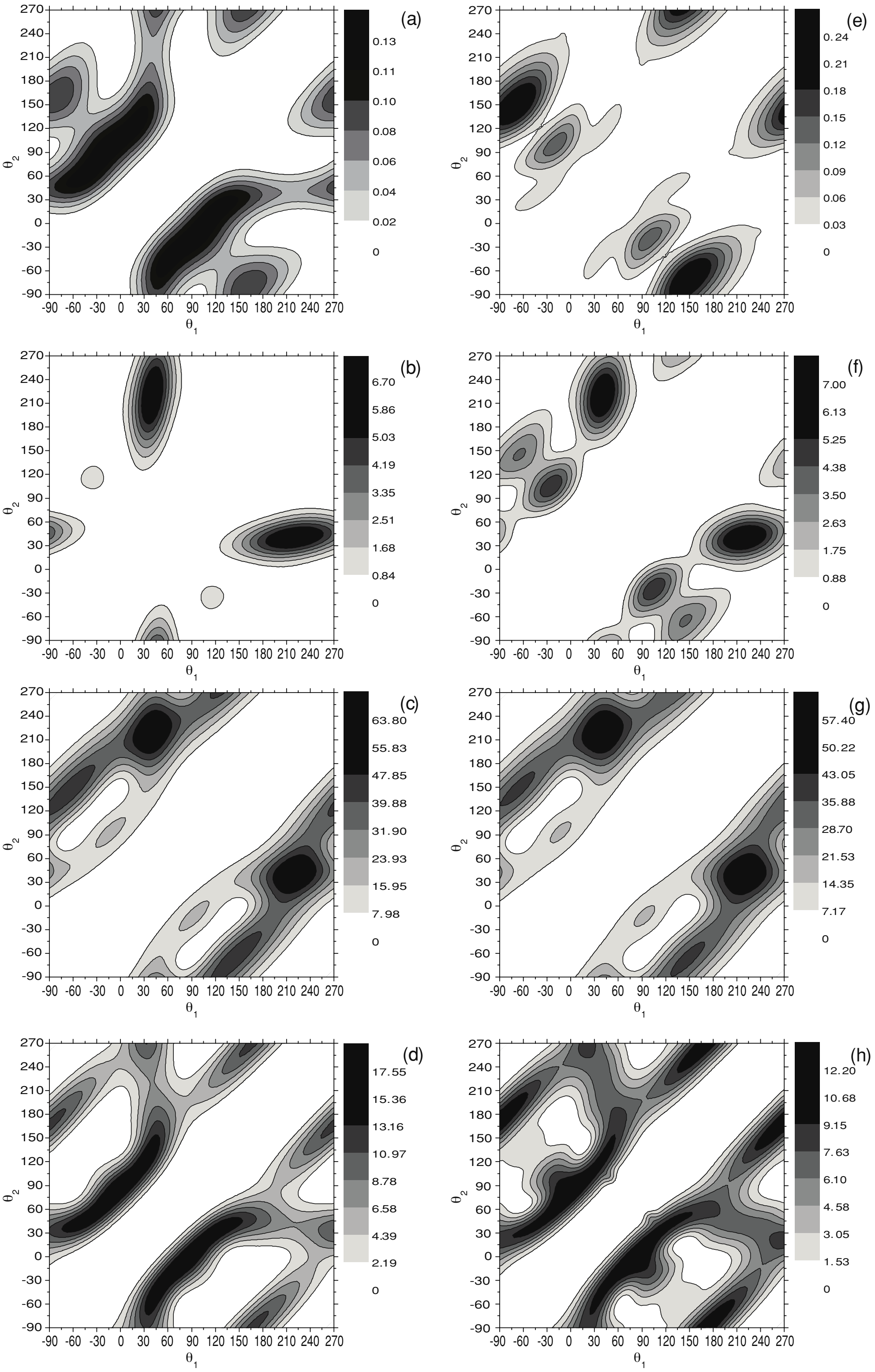

FIG. 1. Angular distributions of the two ejected electrons in the scattering plane. The polar angles are measured from the direction of the incident beam. The calculated ionization FDCSs are given in units of $10^{-6}$ a.u. for proton impinging on He at $E_i = 700$ keV. The electrons are ejected with equal energies of 10 eV and the momentum transfer $Q$ is 0.9 a.u. The contour plots (a)–(d) correspond to the GS1 initial-wave functions, (e)–(h) to the GS2 initial waves. The (a) and (e) plots corresponds to the 2C-Gamow final-state wave function, (b) and (f) to the DS2C-Gamow, (c) and (g) to the 3C, and (d) and (h) to the DS3C model.

FDCSs obtained with different models for the final state and a GS1 initial state and at Figs. 1(e)–1(h) those corresponding to a GS2 initial state for 700-keV proton impact. The emitted electron energies are $E_1 = E_2 = 10\,\text{eV}$ and the momentum transferred by the projectile is $Q = 0.9$ a.u. and $\theta_Q = 40.18^\circ$. The main purpose of this analysis is to contrast the angular distributions of the models so far used to describe the present problem [22–24], which are based on the use of correlation factors, against those obtained by more elaborated models. It can be seen that in the simplest model under consideration (GS1-2C-Gamow), the emission of both electrons in the same direction is strongly suppressed by the Gamow factor which introduces a wide gorge that runs through the diagonal $\theta_1 = \theta_2$, probably overestimating the exclusion mechanism. The introduction of either angular correlation in the initial state [GS2-2C-Gamow, Fig. 1(e)] or DS-effective charges within the 2C-Gamow model [Fig. 1(b)] drastically alters the structures. This clearly highlights the sensitivity of the present system to how the electronic correlation is introduced in both initial and final states. As the final-state correlation is improved by using the 3C and DS3C models, which explicitly consider the $r_{12}$ dependence at the wave-function level, the sensitivity to the initial state is not that large and the distributions obtained by using either GS1 or GS2 are rather similar. Besides, we point out that the FDCS obtained by using the 2C-Gamow final state are two orders of magnitude below those obtained with the more sophisticated 3C and DS3C final states. It is well known that the Gamow factor leads to the underestimation of the double ionization total cross section when associated to the IEL model [14]. It should be expected then that such underestimation would find its origin at the FDCS level in concordance with our results. Interestingly, the introduction of the DS charges of Berakdar and Briggs in the 2C-Gamow model partially corrects such behavior and provides absolute magnitudes much closer to those obtained with the more elaborate models. The effective charges given by Eq. (12) take constant values on the lines where $\theta_2 - \theta_1$ is a constant. In particular $Z^{\mathrm{DS}}_{e_1-e_2}$ is zero along the line where $\theta_2 - \theta_1 = \pi$ and the corresponding Gamow factor is 1. This limit corresponds to the collinear emission configuration in which both electrons leave the reaction region seeing a nuclear charge equal to $Z - 1/4$. Studies performed in the $(e,3e)$ context [36] clearly show that the DS3C model is in much better agreement with the available data than the pure 3C model. In any case, from the inspection of these figures one can conclude that the results obtained by means of the GS2-DS3C model cannot be accurately reproduced by any combination based on the simpler models currently under study for the final state.

An alternative way to explore why the different models exhibit structures at different angular regions is through the inspection of the recoil momentum acquired by the nucleus. In Fig. 2 the contour lines of the FDCS above shown for the GS2 initial state and the 2C-Gamow, DS2C-Gamow, 3C, and DS3C final states, are drawn over the recoil momentum

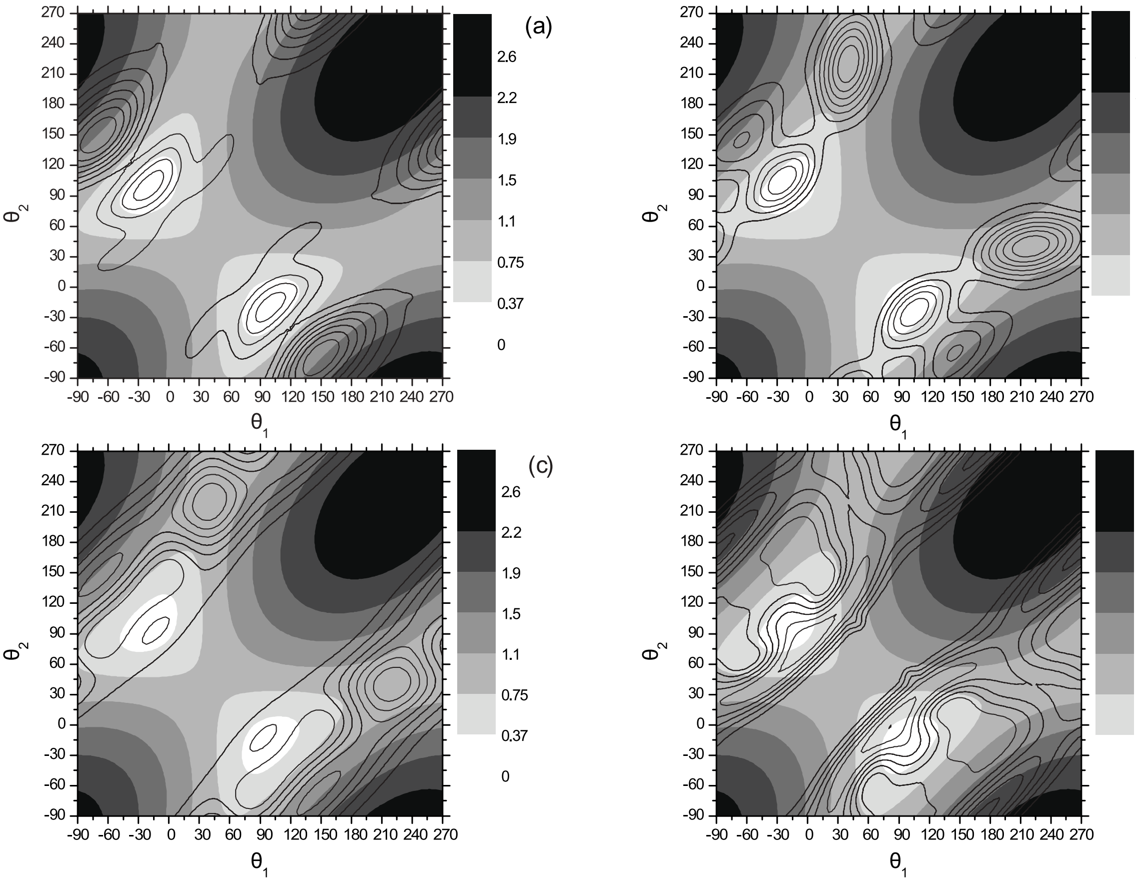

FIG. 2. Angular distributions of the two electrons drawn over the corresponding absolute values of the target recoil momentum, for the same dynamical conditions considered in Fig. 1. The scale on each plot indicates absolute values for the target recoil momentum. Theories: (a) GS2-2C-Gamow, (b) GS2 -DS2C-Gamow, (c) GS2-3C, and (d) GS2-DS3C.

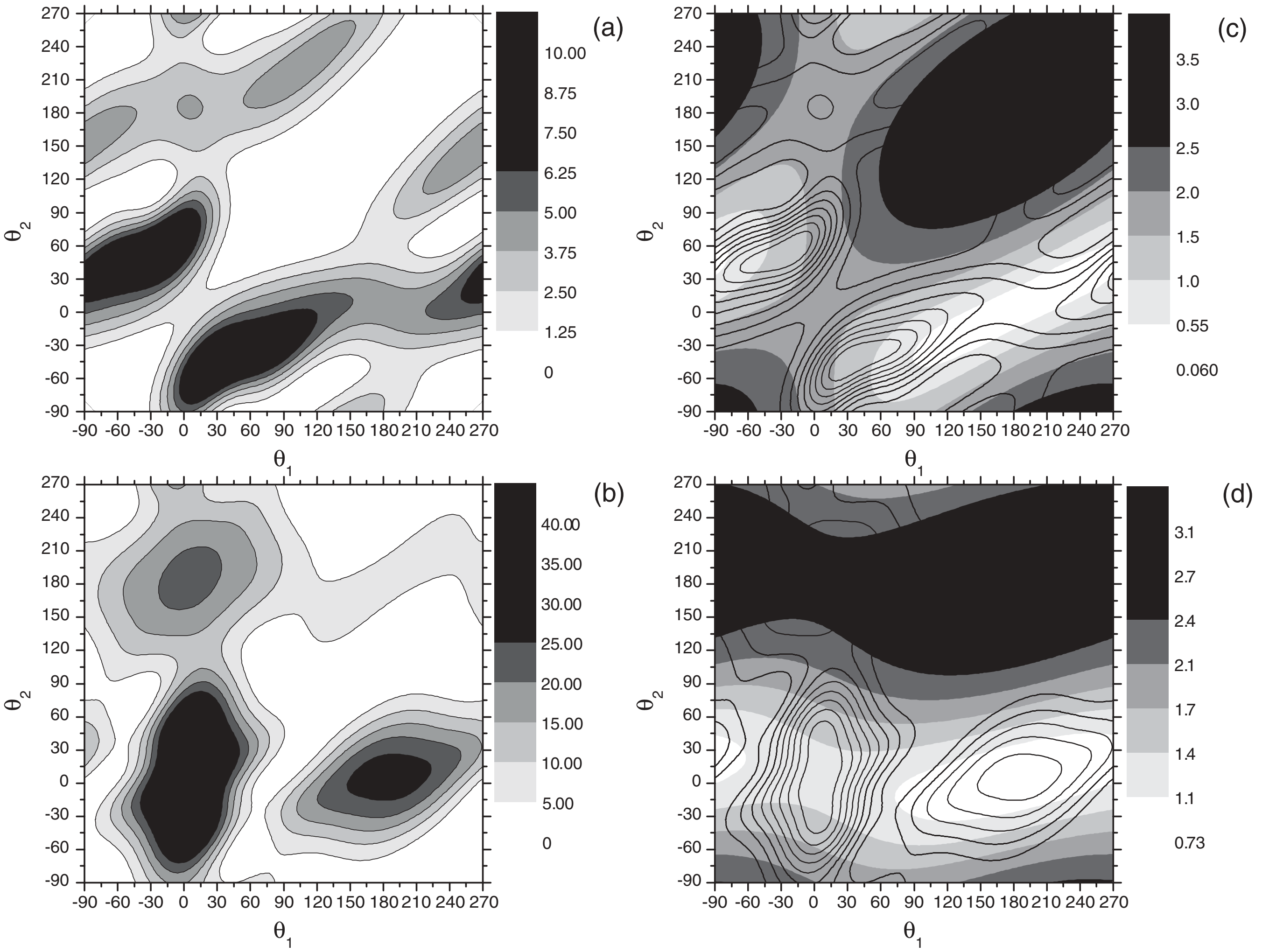

FIG. 3. Contour plots for the scattering plane angular distributions of the two electrons (a), (b) and target recoil (c), (d) for double ionization of He by 700 keV/amu proton impact. The momentum transfer is $Q = 0.9$ a.u. and the energy shared among the electrons is 50 eV. All the calculations were performed with the GS2-DS3C model. The FDCSs are in units of $10^{-6}$ a.u. The different emission geometries considered are (a) and (c) $E_1 = 10$ eV and $E_2 = 40$ eV; (b) and (d) $E_1 = 1$ eV and $E_2 = 49$ eV.

contour plot. The target recoil is obtained from the momentum conservation equation

$$\mathbf{R} = \mathbf{Q} - \mathbf{k}_1 - \mathbf{k}_2 \tag{17}$$

The magnitude of the recoil can be inferred from the scale that is located on the side of each plot. For the GS2-2C-Gamow model, we can identify two main structures: one located at $\theta_1 \approx -15^\circ$ and $\theta_2 \approx 100^\circ$, which represents electrons that tend to leave the reaction region sharing almost all the transferred momentum by the projectile ($\mathbf{k}_1 + \mathbf{k}_2 \approx \mathbf{Q}$), with the target nucleus being practically a witness. The other important structure is seen at $\theta_1 \approx -75^\circ$ and $\theta_2 \approx 150^\circ$, emission geometry for which the recoil acquired by the target nucleus is close to $2\mathbf{Q}$ (position in which the recoil peak would be expected in a single ionization process). Symmetric structures to the ones described are observed with respect to the diagonal $\theta_1 = \theta_2$. The introduction of the DS charges in the 2C-Gamow model drastically alters the distributions: The first structure ($\mathbf{k}_1 + \mathbf{k}_2 \approx \mathbf{Q}$) is already present, but now a strong structure is found close to $\theta_1 \approx 40^\circ$ and $\theta_2 \approx 220^\circ$, which represents the two electrons leaving in a collinear configuration (i.e., with $\mathbf{k}_1 + \mathbf{k}_2 \approx 0$) while the target nucleus absorbs the momentum transfer $\mathbf{Q}$. For the fully correlated final states, we find the GS2-3C model pushing this very last picture (most of the electrons leaving the reaction region in a collinear configuration), which could be in principle expected since during their emission the two electrons (as a two-body subsystem) are unaware of the presence of the recoil nucleus.

The GS2-DS3C, on the other hand, smoothly moderates the two-body interactions taking into account the third particle and as a result we observe that the dominant structures correspond to the binary and recoil peak. This would seem at first sight similar to the GS1-2C-Gamow description but we again point out that there is a difference of two orders of magnitude among theories. Besides, a closer inspection of the region near the diagonal $\theta_1 \approx \theta_2$ shows that it seems to narrow for the GS2-DS3C model compared to the GS1-2C-Gamow model. In terms of the recoil momentum, we observe that the main structure is now centered at $\theta_1 \approx -5^\circ$ and $\theta_2 \approx 85^\circ$, indicating that both electrons can get angularly closer than predicted by

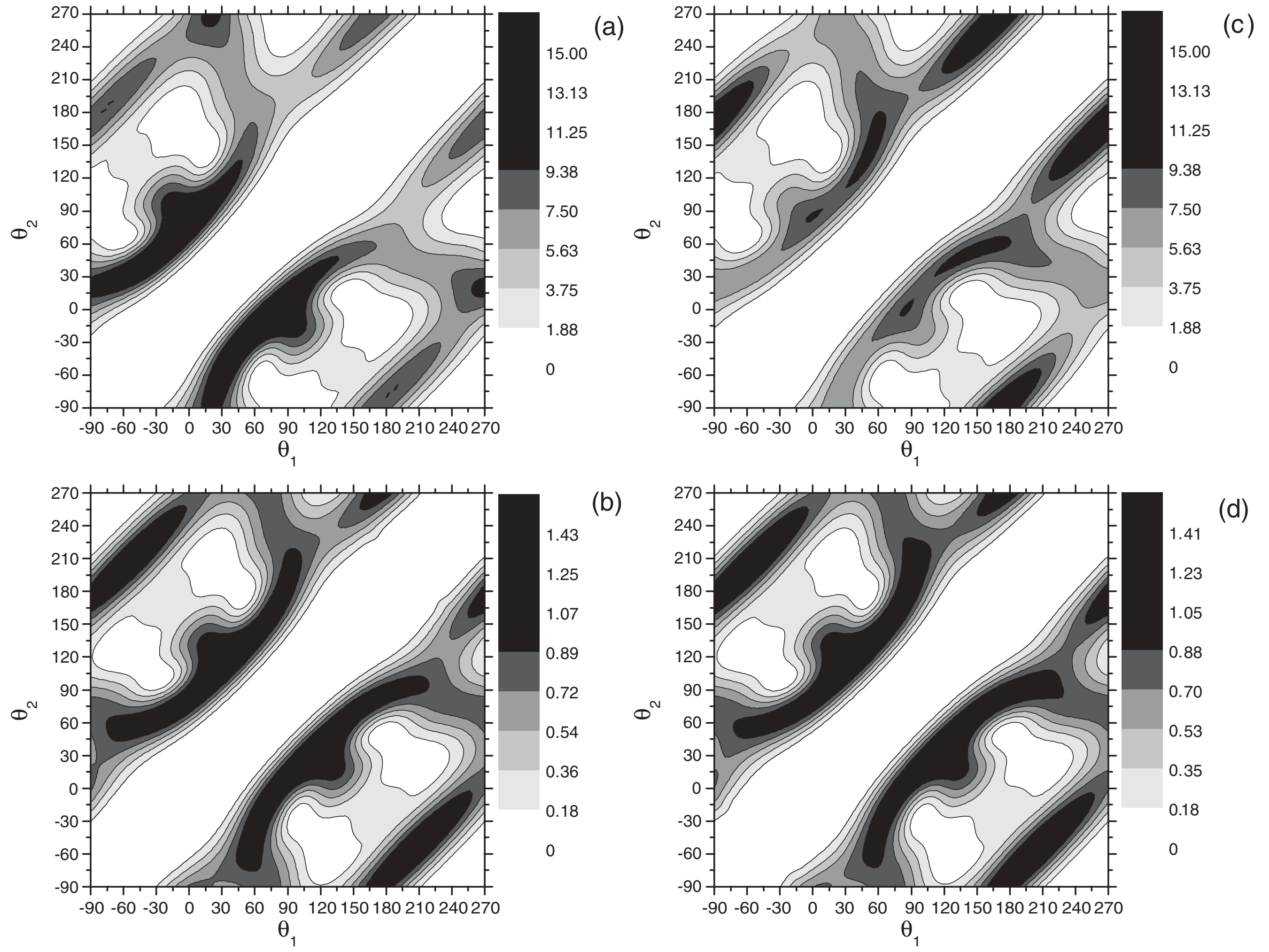

FIG. 4. Contour plots of the angular distributions of the two electrons for double ionization of He by proton impact (a), (b) and antiproton impact (c), (d). The impact energies considered are $E_i = 700$ keV (a) and (c), and $E_i = 6000$ keV (b) and (d). All the calculations were performed with the GS2-DS3C-GO model. The emission geometry considered is that of Fig. 1. The FDCS are in units of $10^{-6}$ a.u.

the GS1-2C-Gamow model. In fact, this peak is placed in an extended ridge that developed along the line $\theta_2 \approx \theta_1 + \pi/2$ indicating that this reaction results when the projectile hits one electron, which pushes out the second one, sharing during the process some momentum with the core. The above described features indicate that the use of the Gamow factor as the only factor in the wavefunction which takes account of the electron-electron interaction, leads to an overestimation of the repulsion effects. In the DS models, the electron-electron interaction is softened in terms of the relative emission angle compared to the pure Gamow factor, providing, in principle, a much more realistic description at least based on physical grounds. Besides, the GS2-DS3C model, through the explicit $r_{12}$ dependence and DS charges, leaves fingerprints at the FDCS level of the role played by the electron-electron repulsion that could be traced, in principle, by inspection of the recoil momentum.

In Fig. 3 we consider the double ionization of He by a 700-keV proton impact for different sharings of the total emission energy among the electrons. The theoretical model chosen for this study is the GS2-DS3C. This model satisfies more desirable physical limits than any other possible combination based on the wave functions above shown. The momentum transfer is $Q = 0.9$ a.u. and $\theta_Q = 10.26^\circ$, the emission energy shared among the two electrons is 50 eV, and the FDCS distributions obtained are shown for $E_1 = 10$ eV and 1 eV in the first column. In the second column selected contour levels are drawn over the recoil momentum contour plot to help visualize the main physical trends that can be inferred for the different energy sharings. For $E_1 = 10$ eV and $E_2 = 40$ eV, the main yield appears for $\theta_2 \approx \theta_1 + \pi/2$. A possible interpretation would be provided by the projectile hitting one electron, which then collides with the core and pushes out the second electron. As the electron emission energies turn more asymmetric, we observe that the probability of finding electrons emitted in the forward direction increases (i.e., the dynamic restriction remnants from the equal energy distribution get lost as the energy sharing is more asymmetric). For $E_1 = 1$ eV and $E_2 = 49$ eV, the recoil distribution patterns tend to conform to two horizontal strips, which can be related to large and low recoil momentum respectively. From these strips we infer that in terms of acquired momentum, the

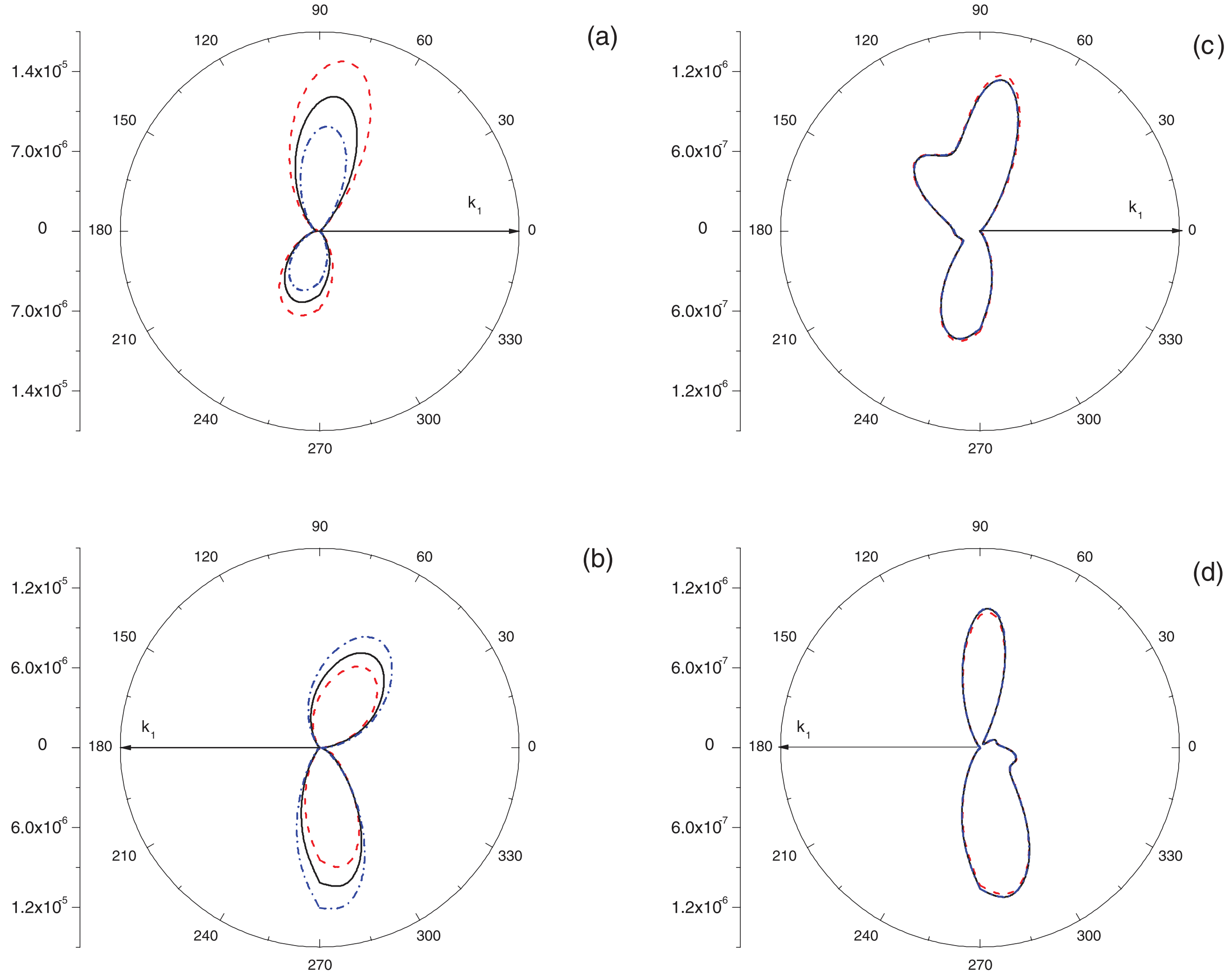

FIG. 5. (Color online) Selected cuts of the surfaces shown in Fig. 4 represented in terms of polar plots from for: (a), (b) $E_i = 700$ keV and (c), (d) $E_i = 6000$ keV. Angular distributions for one of the emitted electrons are shown at fixed emission angles of the other one at values (a) and (c) $\theta_1 = 0^\circ$, and (b) and (d) $\theta_1 = 180^\circ$ (indicated by arrows). Theories: GS2-DS3C model (solid line); GS2-DS3C-GO model for proton impact (dashed line); GS2-DS3C-GO model for antiproton impact (dashed-dotted line).

target nucleus is rather sensitive (insensitive) to the emission direction of the fast (slow) electron. From Fig. 3, we notice that most of the double emission is in this case associated to low momentum transfer to the target nucleus, with both electrons being emitted in the forward direction ($\theta_1,\theta_2 < 90^\circ$). Other structures are found around $\theta_1 \approx 0^\circ$ and $\theta_2 \approx 180^\circ$, in which the fast electron suffers a strong interaction with the recoiling nucleus, and $\theta_1 \approx 180^\circ$ and $\theta_2 \approx 0^\circ$, which can be related to the fast electron departing in the forward direction and the slow electron interacting with the recoiling nucleus. Concerning magnitudes, we notice that the FDCS magnitudes for the most asymmetric double emission here considered are about a factor of 5 greater than those corresponding to the equal energy case. This should be relevant at the integrated cross sections level. Although not shown here, for the equal energy case corresponding to $E_1 = 25$ eV and $E_2 = 25$ eV, the angular distribution is similar to Fig. 1(h) and the same comments apply.

We now turn our attention to the projectile field effects on the FDCS and describe the results obtained by means of the GS2-DS3C-GO model. The effective charges in this model depend on the relative velocities of the four particles, introducing multiple collisions in the reaction zone, which is equivalent to the introduction of higher-order perturbative corrections in the present first Born approximation. In Fig. 4 we compare the double emission distributions in the collision plane for proton and antiproton collisions at impact energies of 700 keV and 6000 keV. Selected cuts of these surfaces are shown in terms of polar plots in Fig. 5. The emitted electron energies and momentum transfer are those considered in Fig. 1. Clear differences are observed in the structures predicted for both projectiles at the lowest energy considered of 700 keV. Compared to the GS2-DS3C model [Fig. 1(h)] the structure associated to recoil values close to $2Q$ is enhanced for antiproton impact and weakened for proton impact. This is clearly shown in Fig. 5(b) and can be explained in terms of the

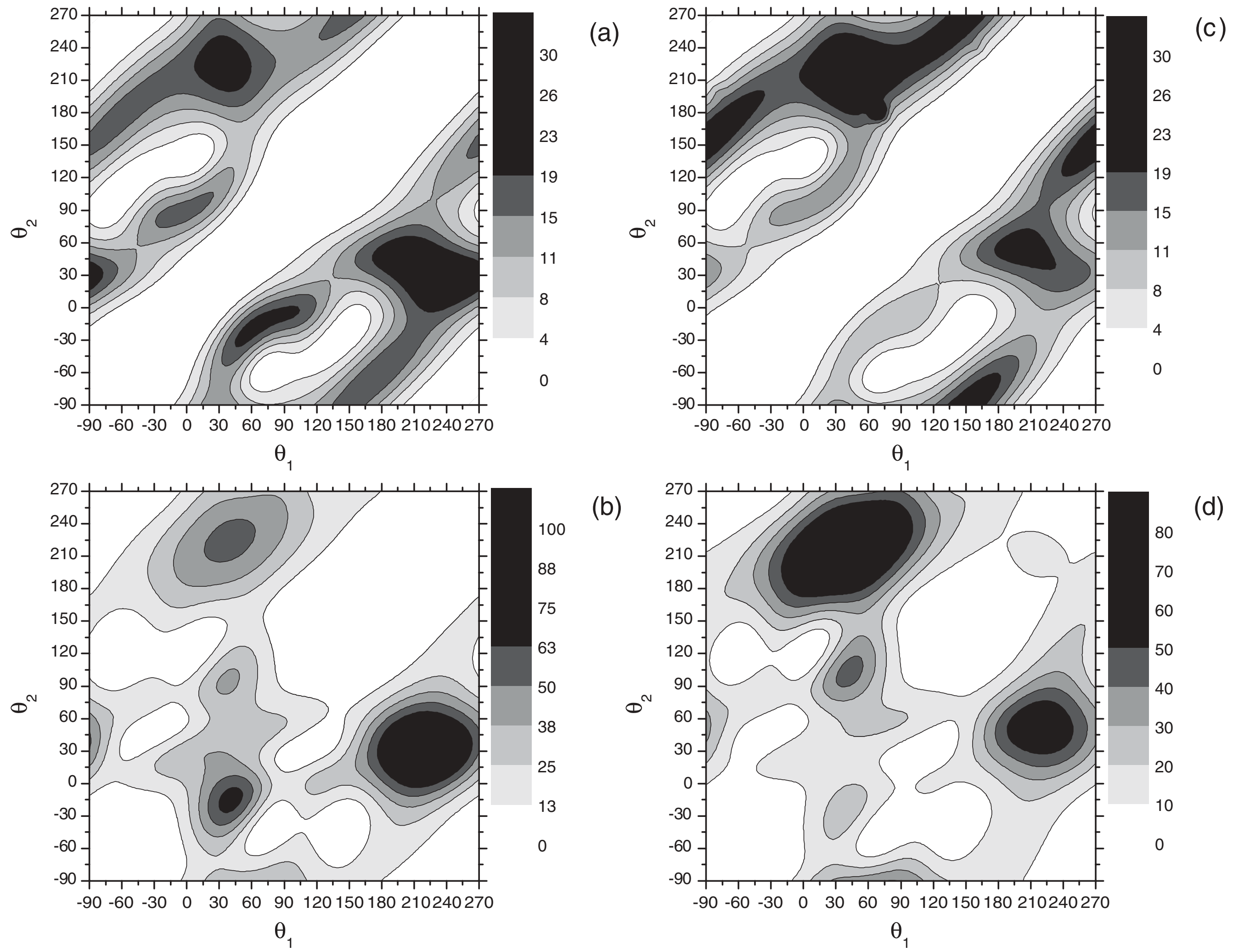

FIG. 6. Contour plots of the angular distributions of the two emitted electrons for proton (a), (b) and antiproton (c), (d) impact. All the particles are in the scattering plane and the electrons are emitted with asymmetric energies. The calculations were performed with the GS2-DS3C-GO model, and the FDCSs are given in units of $10^{-6}$ a.u. The collision energy is $E_i = 700$ keV, the momentum transfer $Q = 0.9$ a.u. and the different emission geometries considered are (a) and (c) $E_1 = 5$ eV and $E_2 = 15$ eV; (b) and (d) $E_1 = 1$ eV and $E_2 = 19$ eV.

decrease (increase) of the target charge seen by the electrons for proton (antiproton) impact, which provides the physical picture of the electrons being pulled from (pushed against) the target nucleus by the receding projectile.

Similar conclusions apply for the structures seen at $\theta_1 \approx 0^\circ$ and $\theta_2 \approx 80^\circ$ for proton impact. In this case, the picture of a binary collision between the projectile with one of the electrons, which in a subsequent collision ejects the other electron becomes clearly evident. In the latter, on the other hand, it is clearly observed that the receding projectile favors the interaction of the emitted electrons with the target nucleus as inferred from the recoil momentum acquired. These plots highlight the statements above discussed and allow a closer inspection of the structures. In all cases, the GS2-DS3C model results lay in between the proton and antiproton results. As expected, the differences tend to vanish as the impact energy increases. At the impact energy of 6000 keV, the present FDCS for proton and antiproton impact are very similar and already converge to the GS2-DS3C, as shown in Figs. 5(c) and 5(d).

In Fig. 6 we consider the unequal energy sharing case for a total excess energy of 20 eV. The FDCS for $E_1 =$ 5 eV and 1 eV are shown for 700 keV/amu proton impact (first column) and antiproton impact (second column). The momentum transferred by the projectile is set equal to 0.9 a.u. and $\theta_Q = 40.18^\circ$, as in Fig. 1. As above stated, the cross sections turn more intense as the electron emission energies become more asymmetric. For proton impact and $E_1 = 5$ eV we observe a large part of the emission in a geometry that corresponds to the fast electron being ejected at $\theta_2 \approx 30^\circ$ while the slow electron departs at $\theta_1 \approx 240^\circ$ (i.e., the proton drags the fast electron). We notice that this particular structure turns dominant as the energy asymmetry among electrons increases. A weaker cusp is observed around $\theta_1 \approx 30^\circ$ and $\theta_2 \approx 220^\circ$, which can be associated to a second-order collision with the target by the fast electron. For antiproton impact on the other hand, the most intense structure is found around $\theta_1 \approx 45^\circ$ and $\theta_2 \approx 220^\circ$ indicating that the fast electron prefers backward emission angles. This structure turns dominant for

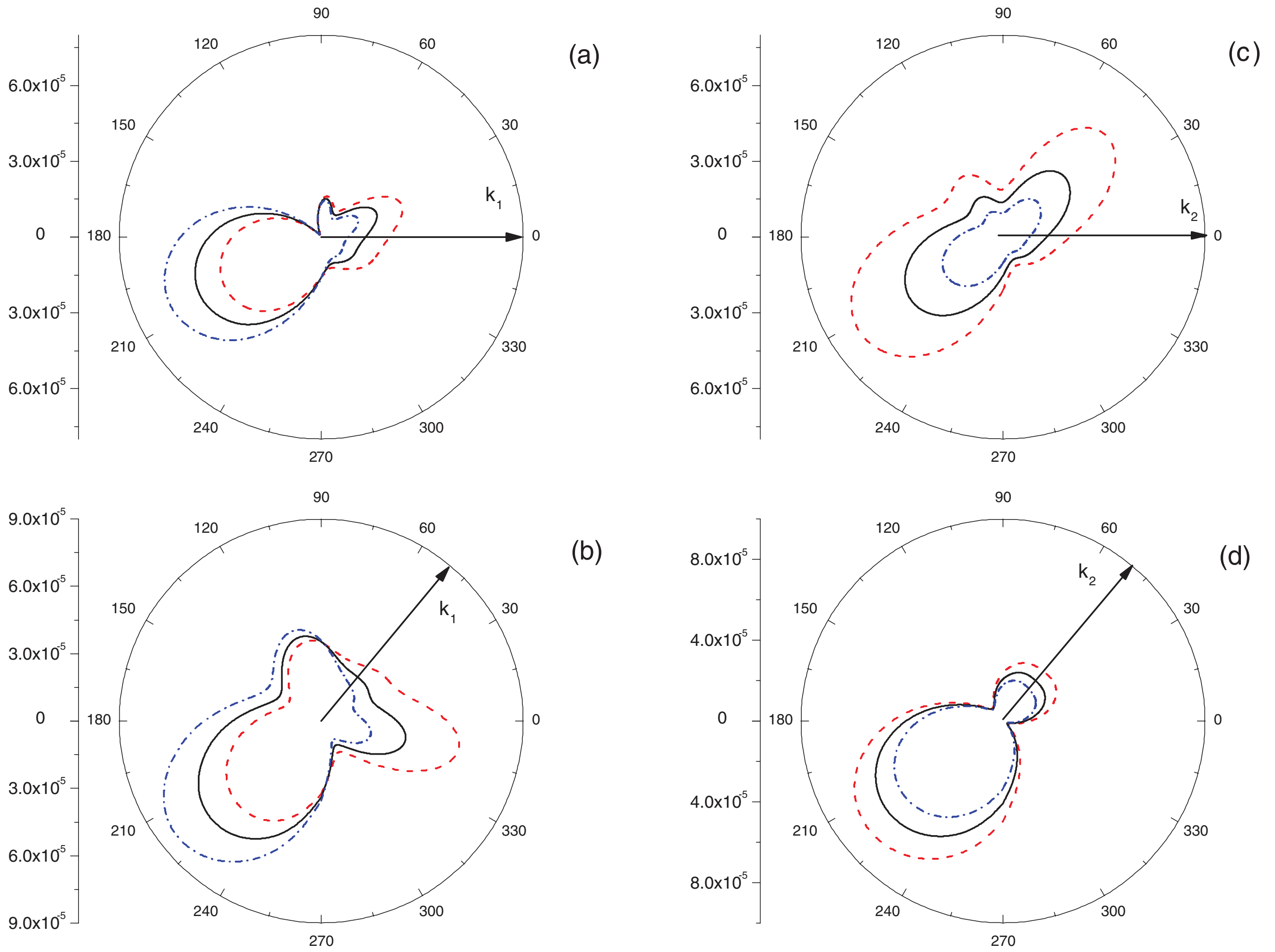

FIG. 7. (Color online) Selected cuts from Figs. 6(b) and 6(d) in polar plot representation. The cuts are taken at fixed momentum of the slow electron (a), (b) $E_1 = 1$ eV, and for the fast electron (c), (d) $E_2 = 19$ eV. The emission angle of one of the electrons is indicated with an arrow at (a) and (c) $\theta_{1,2} = 0^\circ$, and (b) and (d) $\theta_{1,2} = 50^\circ$, respectively. Theories: Same as in Fig. 5.

the most asymmetric energy sharing among electrons under study. Additionally, it can be seen that in all cases double electron emission in the forward direction ( $\theta_1,\theta_2 < 90^\circ$) seems to be strengthened for proton impact and weakened for antiproton impact. In order to perform a closer inspection, in Fig. 7 selected cuts of Fig. 6(b) and 6(d) are shown in polar representation and are compared to the results obtained with the GS2-DS3C model, for the more asymmetric energy case. In the left column we show the fast electron distributions for the slow electron being ejected at angles $\theta_1 = 0^\circ$and 50°. In the right column, on the other hand, we present the slow electron distributions with the fast one being emitted at the angles above mentioned. The first thing to notice in Figs. 7(a) and 7(b) is that the fast electron shows an emission in the forward direction for proton impact larger than for antiproton impact. The postcollisional picture we get is that of the proton pulling the fast emitted electrons, increasing (diminishing) the forward (backward) emission. The inverse situation is observed for antiproton impact.

Similar features were recently described in single ionization of argon by electron and positron impact [39,40]. Since the GS2-DS3C model does not account for any kind of postcollisional interaction between the atomic subsystem and the receding projectile, it provides a clear view of how the structures are altered when using the GS2-DS3C-GO model. We now turn to the slow electron distribution, for which we observe a more intense distribution in the case of proton impact than for antiproton impact. This can be explained by considering that the slow electron electron emission resembles an $(e,2e)$ process, but with the projectile field influencing the size of the target. For proton impact the electron target nucleus interactions are weakened in contrast to the antiproton impact case, where the electron target nucleus interactions are strengthened. As a result, the chance of a second order electron-electron collision is much more probable for proton impact than for antiproton.

In Fig. 8, we consider other projectiles and show the surface distributions for 1 MeV/amu collisions of $\mathrm{He}^{2+}$, $\mathrm{Li}^{3+}$, and $\mathrm{C}^{6+}$ on He. The electron emission energies considered are $E_1 = E_2 = 10$ eV and $Q = 0.9$ a.u. The first thing we note is a ridge resulting from momentum transference from the projectile to one electron which kicks off the other electron and transfers some momentum to the core before being emitted. In this ridge the more intense structure takes place when the

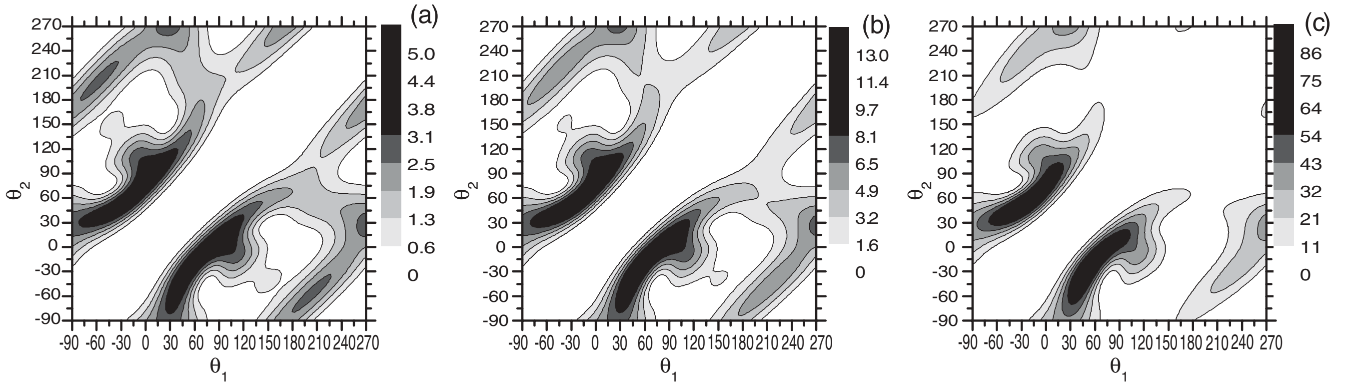

FIG. 8. Contour plots of the angular distributions of the two emitted electrons for (a) $He^{2+}$, (b) $Li^{3+}$, and (c) $C^{6+}$ impact with energy $E_i = 700$ keV/amu. The calculations were performed with the GS2-DS3C-GO model, for $E_1 = E_2 = 10$ eV and $Q = 0.9$ a.u. The FDCSs are in units of $10^{-5}$ a.u.

target nucleus remains still, the situation which corresponds to $\mathbf{k}_1 + \mathbf{k}_2 \approx \mathbf{Q}$. We observe that the structure corresponding to $\mathbf{R} \approx 2\mathbf{Q}$ tends to disappear for large $Z_P$. This would indicate that the second-order interactions with the target nucleus become less important as the impact charge increases. This should be expected since the highly charged projectile is pulling both electrons out, clearly diminishing the probability of a secondary collision between the emitted electrons with the

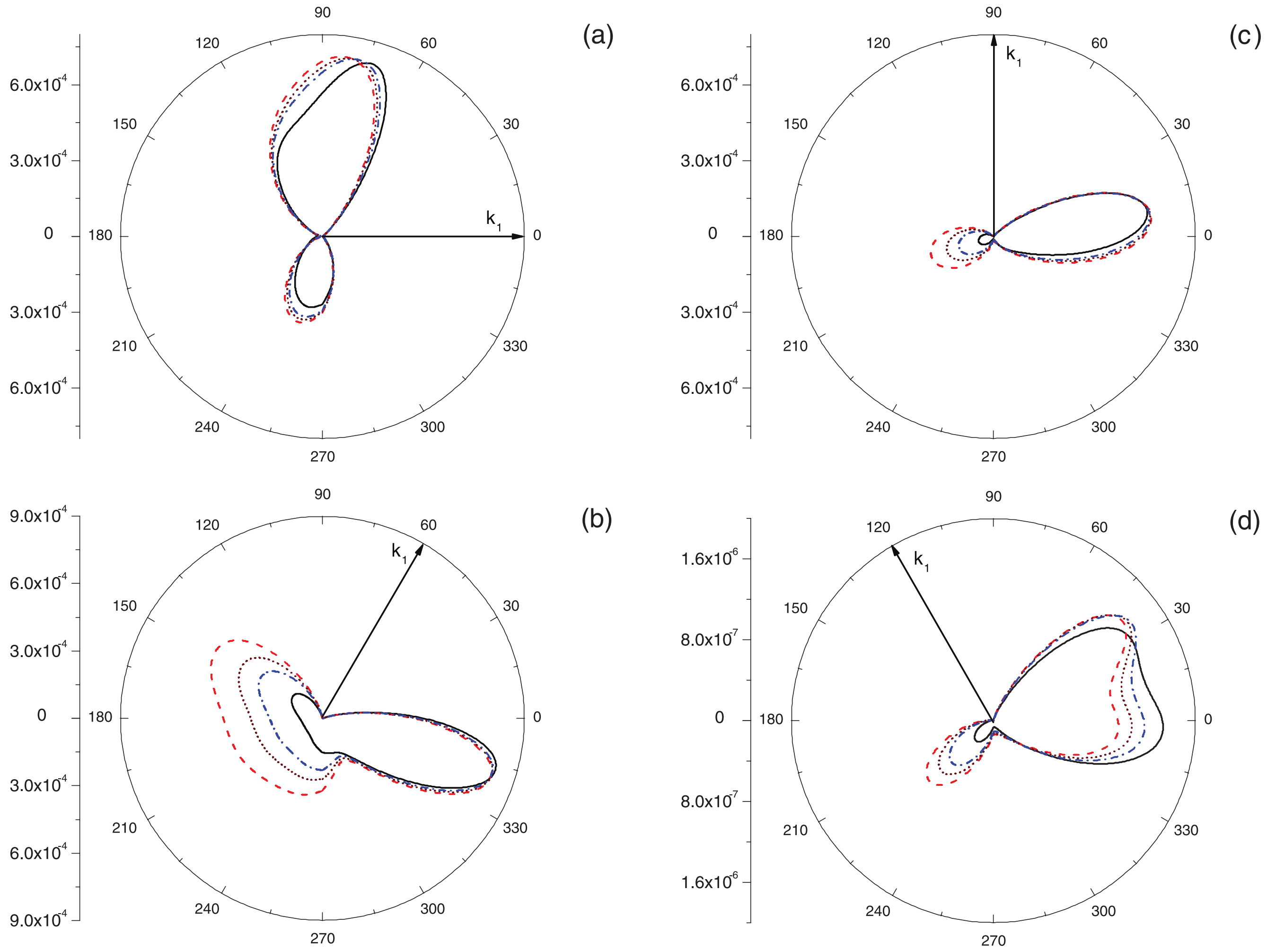

FIG. 9. (Color online) Selected cuts of Figs. 8(a)–8(c) in polar plot representation with the addition of data for proton impact. The theoretical method, impact energy, momentum transfer, and electron energies are as in Fig. 8. The emission angle of one of the electrons is indicated with an arrow at (a) $\theta_1 = 0^\circ$, (b) $\theta_1 = 60^\circ$, (c) $\theta_1 = 90^\circ$, and (d) $\theta_1 = 120^\circ$. $C^{6+}$ impact (solid line), proton impact (dashed line), $He^{2+}$ impact (dotted line), and $Li^{3+}$ impact (dashed-dotted line). For a better visualization, all curves are normalized to the FDCS obtained for $C^{6+}$ impact.

target. In Fig. 9 we show polar plots corresponding to selected cuts of these surfaces and we add the proton impact data. The second electron distribution is studied as a function of the first electron emission angle. The different curves have been normalized to the highest structure for $C^{6+}$ in order to compare the angular profiles. It can be seen that the second-order interactions with the target nucleus clearly tend to diminish as the projectile charge increases as above stated. Furthermore, the peaks corresponding to emission geometries for which the target nucleus plays a minor role are strongly influenced as can be inferred from the shape distortion and the emission profiles which are tilted toward the projectile direction $\theta \approx 0^\circ$. All this theoretical evidence highlights the importance of having a model able to include the postcollisional interaction between the receding projectile and the He subsystem fragments at the collision energies under consideration.

## IV. CONCLUSIONS

In this work we have theoretically studied the double ionization of He by protons, antiprotons and fully stripped ions. Fully differential cross sections have been calculated using a distorted wave model that allowed the implementation of different wave functions for the initial and final states of the He subsystem. A relevant theoretical advance is attained by describing the final state with a full 3C wave function, improving former descriptions based on the 2C wave together with a simple Gamow factor to account for the *e*-*e* correlation. Since the static charges in the 3C model do not account for the dynamical screening produced by the relative motion of the four particles in the final state, we have introduced two distorted wave methods based on dynamically screened charges. The first model considers the dynamical correlation between the electrons and the target nucleus, assuming the effective charges proposed by Berakdar [33]. The second model additionally incorporates the influence of the receding projectile following the proposal of Jetzke and Faisal [25]. Basically, the field of the receding projectile alters the way in which the emitted electrons interact with the recoiling target nucleus.

The probability of a secondary interaction between the emitted electrons and the target nucleus is increased in the case of antiproton impact and diminished for positive ion impact. The present results suggest that double emission for asymmetric electron energies is much more favorable than equal energy double emission. Furthermore, we have shown that from the inspection of the recoil momentum acquired by the target nucleus it can be possible to gain insight on the He subsystem dynamics predicted by the different models.

Fully stripped projectiles with charges up to 6+ have been considered and found to strongly influence the electronic angular distributions at the impact energy of 1 MeV/amu. As the projectile charge increases, the electronic distributions are more localized and, as stated above, the chance that the electrons suffer a secondary collision with the target nucleus tends to vanish.

We found that the calculated FDCSs for proton and antiproton impact with the GS2-DS3C-GO model clearly differ at the lowest impact energy here considered (700 keV/amu) but differences tend to disappear as the impact energy is increased. It is well known from the $\sigma^{2+}/\sigma^{+}$ studies performed in the 1980s that at 6 MeV/amu the antiproton $\sigma^{2+}$ cross sections are expected to almost duplicate those obtained with protons. Within the GS2-DS3C-GO model, as the impact energy is increased to 6 MeV/amu, the results for proton and antiproton impact are almost indistinguishable and converge to the GS2-DS3C results. Whether this is a consequence of the limitations of the model under consideration or a characteristic of the limit of intermediate- to low-momentum transfers here considered remains an open issue. A second Born approximation model for the present collision system is currently under way and will be contrasted against the present model.

We hope this work will give guidance and stimulate future experimental work to further refine our understanding of these collision systems at the fully differential level.

## ACKNOWLEDGMENTS

This work was supported by the Universidad Nacional del Sur, Grant No. PGI 24/F049, the Agencia Nacional de Promoción Científica y Tecnológica, Grant No. PICT 2007-00887, and the Consejo Nacional de Investigaciones Cientificas y Tecnicas, Grant No. PIP 112-200801-02760.

---

[1] T. E. Cravens, Science **296**, 1042 (2002).
[2] S. Otranto, R. E. Olson, and P. Beiersdorfer, J. Phys. B **40**, 1755 (2007).
[3] B. Gervais, M. Beuve, G. H. Olivera, and M. E. Galassi, Radiat. Phys. Chem. **75**, 493 (2006).
[4] M. B. Shah and H. B. Gilbody, J. Phys. B **18**, 899 (1985).
[5] L. H. Andersen, P. Hvelplund, H. Knudsen, S. P. Moller, K. Elsener, K. G. Rensfelt, and E. Uggerhoj, Phys. Rev. Lett. **57**, 2147 (1986).
[6] J. F. Reading and A. L. Ford, Phys. Rev. Lett. **58**, 543 (1987).
[7] R. E. Olson, Phys. Rev. A **36**, 1519 (1987).
[8] J. H. McGuire and L. Weaver, Phys. Rev. A **16**, 41 (1977).
[9] M. McCartney, Nucl. Instrum. Methods Phys. Res. B **155**, 343 (1999).
[10] M. Fiori, A. B. Rocha, C. E. Bielschowsky, G. Jalbert, and C. R. Garibotti, J. Phys. B **39**, 1751 (2006).
[11] N. C. Deb and D. S. F. Crothers, J. Phys. B **23**, L799 (1990).
[12] N. C. Deb and D. S. F. Crothers, J. Phys. B **24**, 2359 (1991).
[13] J. Bradley, R. J. S. Lee, M. McCartney, and D. S. F. Crothers, J. Phys. B **37**, 3723 (2004).
[14] L. Gulyás, A. Igarashi, P. D. Fainstein, and T. Kirchner, J. Phys. B **37**, 3723 (2004).
[15] R. Moshammer, M. Unverzagt, W. Schmitt, J. Ullrich, and H. Schmidt-Böcking, Nucl. Instrum. Methods Phys. Res., Sect. B **108**, 425 (1996).
[16] A. Dorn, A. Kheifets, C. D. Schröter, B. Najjari, C. Höhr, R. Moshammer, and J. Ullrich, Phys. Rev. Lett. **86**, 3755 (2001).
[17] D. Fischer *et al.*, Phys. Rev. Lett. **90**, 243201 (2003).
[18] D. Fischer, M. Schulz, R. Moshammer, and J. Ullrich, J. Phys. B **37**, 1103 (2004).
[19] M. Foster, J. Colgan, and M. S. Pindzola, J. Phys. B **41**, 111002 (2008).

[20] X. Guan and K. Bartschat, Phys. Rev. Lett. **103**, 213201 (2009).
[21] S. J. Ward and J. H. Macek, Phys. Rev. A **49**, 1049 (1994).
[22] E. M. Lobanova, S. A. Sheinerman, and L. G. Gerchikov, J. Exp. Theor. Phys. **105**, 486 (2007).
[23] M. F. Ciappina, M. Schulz, T. Kirchner, D. Fischer, R. Moshammer, and J. Ullrich, Phys. Rev. A **77**, 062706 (2008).
[24] D. Fischer *et al.*, Phys. Rev. A **80**, 062703 (2009).
[25] S. Jetzke and S. H. M. Faisal, J. Phys. B **25**, 1543 (1992).
[26] R. A. Bonham and D. A. Kohl, J. Chem. Phys. **45**, 2471 (1966).
[27] S. Otranto, G. Gasaneo, and C. R. Garibotti, Nucl. Instrum. Methods Phys. Res., Sect. B **217**, 12 (2004).
[28] C. R. Garibotti and J. E. Miraglia, Phys. Rev. A **21**, 572 (1980).
[29] M. Brauner, J. S. Briggs, and H. Klar, J. Phys. B **22**, 2265 (1989).
[30] S. Otranto and C. R. Garibotti, Eur. Phys. J. D **21**, 285 (2002).
[31] E. O. Alt and A. M. Mukhamedzhanov, Phys. Rev. A **47**, 2004 (1993).
[32] J. Berakdar and J. S. Briggs, Phys. Rev. Lett. **72**, 3799 (1994).
[33] J. Berakdar, Phys. Rev. A **53**, 2314 (1996); **54**, 1480 (1996).
[34] G. Gasaneo, F. D. Colavecchia, C. R. Garibotti, J. E. Miraglia, and P. Macri, Phys. Rev. A **55**, 2809 (1997).
[35] J. E. Miraglia, M. G. Bustamante, and P. A. Macri, Phys. Rev. A **60**, 4532 (1999).
[36] J. R. Götz, M. Walter, and J. S. Briggs, J. Phys. B **39**, 4365 (2006).
[37] A. Lahmam-Bennani, E. M. Staicu-Casagrande, A. Naja, C. Dal Capello, and P. Bolognesi, J. Phys. B **43**, 105201 (2010).
[38] G. Gasaneo, S. Otranto, and K. V. Rodriguez, *Proceedings of the 24th International Conference on Photonic, Electronic, and Atomic Collisions* (World Scientific, Singapore, 2006), p. 360.
[39] S. Otranto and R. E. Olson, Phys. Rev. A **80**, 012714 (2009).
[40] O. G. de Lucio, S. Otranto, R. E. Olson, and R. D. DuBois, Phys. Rev. Lett. **104**, 163201 (2010).